



HAL
open science

Forcing mechanisms governing diurnal, seasonal, and interannual variability in the boundary layer depths: Five years of continuous lidar observations over a suburban site near Paris

Sandip Pal, Martial Haeffelin

► **To cite this version:**

Sandip Pal, Martial Haeffelin. Forcing mechanisms governing diurnal, seasonal, and interannual variability in the boundary layer depths: Five years of continuous lidar observations over a suburban site near Paris. *Journal of Geophysical Research: Atmospheres*, 2015, 120, pp.11,936-11,956. 10.1002/2015JD023268 . hal-04114662

HAL Id: hal-04114662

<https://hal.science/hal-04114662>

Submitted on 5 Jun 2023

HAL is a multi-disciplinary open access archive for the deposit and dissemination of scientific research documents, whether they are published or not. The documents may come from teaching and research institutions in France or abroad, or from public or private research centers.

L'archive ouverte pluridisciplinaire **HAL**, est destinée au dépôt et à la diffusion de documents scientifiques de niveau recherche, publiés ou non, émanant des établissements d'enseignement et de recherche français ou étrangers, des laboratoires publics ou privés.

Copyright

RESEARCH ARTICLE

10.1002/2015JD023268

Key Points:

- Continuous, long-term, high-resolution time series of lidar-derived ABL depths
- Impacts of near-surface thermodynamics and meteorological conditions on ABL
- Seasonal, interannual variability in ABL depths and meteorological conditions

Correspondence to:

S. Pal,
sp5hd@virginia.edu;
sup252@psu.edu

Citation:

Pal, S., and M. Haeffelin (2015), Forcing mechanisms governing diurnal, seasonal, and interannual variability in the boundary layer depths: Five years of continuous lidar observations over a suburban site near Paris, *J. Geophys. Res. Atmos.*, 120, 11,936–11,956, doi:10.1002/2015JD023268.

Received 17 FEB 2015

Accepted 5 NOV 2015

Accepted article online 9 NOV 2015

Published online 4 DEC 2015

Forcing mechanisms governing diurnal, seasonal, and interannual variability in the boundary layer depths: Five years of continuous lidar observations over a suburban site near Paris

Sandip Pal^{1,2} and Martial Haeffelin³

¹Laboratoire de Météorologie Dynamique, CNRS-Ecole Polytechnique, Palaiseau, France, ²Now at Department of Environmental Sciences, University of Virginia, Charlottesville, Virginia, USA, ³Institut Pierre-Simon Laplace, CNRS-Ecole Polytechnique, Paris, France

Abstract The atmospheric boundary layer (ABL) depth, z_i , is a fundamental variable of ABL and a climatologically important quantity. The exchange of energy between the Earth's surface and the atmosphere is governed by turbulent mixing processes in the daytime ABL, and thus, z_i is important for scaling turbulence and diffusion in both meteorological and air quality models. A long-term data set of z_i was derived at the Site Instrumental de Recherche par Télédétection Atmosphérique (SIRTA) observatory near Paris, using measurements obtained from a ground-based vertically pointing aerosol lidar and an autonomous algorithm STRAT+. Using multiparameter observational data sets covering a 5 year period (October 2008 to September 2013), this study aims to explore two interconnected ABL research topics: brief climatology involving multiscale temporal z_i variability (diurnal, seasonal, annual, and interannual) and the relationship between z_i and near-surface thermodynamic parameters to determine meteorological processes governing z_i variability. Both the z_i and the growth rate over SIRTA showed large seasonal variability with higher mean values in spring (1633 m and 225 m h⁻¹) and summer (1947 m and 247 m h⁻¹) than in autumn (1439 m and 196 m h⁻¹) and winter (1033 m and 149 m h⁻¹). Seasonal variability of daytime maximum z_i is found to be strongly and linearly correlated with downwelling solar radiation at the surface ($r = 0.92$), while the dependence between daytime maximum z_i and sensible heat flux (SHF) at seasonal scales is not fully linear, in particular, for summer months. Interannual variability is studied using deseasonalized monthly-mean anomalies of each variable. Conditional sampling and linear regression analyses between the anomalies of deseasonalized SHF and daytime maximum z_i show (1) stronger correlation between the two parameters for the soil conditions compared to the wet soil conditions, (2) that z_i anomalies were more dependent on SHF anomalies for negative than for positive boundary layer wind speed anomalies, and (3) in the summer season, z_i anomalies varied more consistently with SHF anomalies for conditions with negative cloud cover anomalies than in conditions with positive cloud cover anomalies.

1. Introduction

The development and maintenance of the atmospheric boundary layer (ABL) plays a key role in governing the distribution of atmospheric constituents like aerosols, greenhouse gases (GHG), water vapor, ozone, and radon and controls the atmospheric processes like convective activity, entrainment, fog, cloud, and aerosol formation [e.g., Stull, 1988; Nilsson et al., 2001; Haeffelin et al., 2012; Pal et al., 2014]. Thus, the study of the ABL top height (z_i) variability is important with regard to air quality, climate, and weather forecasting [e.g., Behrendt et al., 2011; Pal et al., 2015; Banks et al., 2015].

To obtain a comprehensive view of the mixing processes of different tracers (e.g., GHG, aerosols, and other trace gases), a better understanding of the combined effects of land surface conditions and z_i variability and growth rate on diurnal, seasonal, and interannual timescales is greatly needed [e.g., Janssen et al., 2012; Lac et al., 2013]. For instance, within ICOS (Integrated Carbon Observing System), a recently launched, world-class research infrastructure, dedicated to provide harmonized high precision measurements for research on carbon cycle and GHG budgets, regular z_i monitoring is considered one of the key tasks [e.g., Haeffelin et al., 2012; Paris et al., 2014].

A detailed understanding of the surface-atmosphere interactions based on long-term measurements of z_i is considered challenging but important for applications like atmospheric transport, dynamics, and chemistry

Table 1. List of Abbreviations for the Different Atmospheric Layers, the Different Sites, the Projects, and the Networks Frequently Used in the Present Study

Abbreviation	Definition
<i>Atmospheric Layers</i>	
ABL	Atmospheric boundary layer
CBL	Convective boundary layer
RL	Residual layer
FA	Free atmosphere
NBL	Nocturnal boundary layer
SBL	Stable boundary layer
<i>Projects, Sites, and Programs</i>	
EARLINET	European Aerosol Research Lidar Network
ICOS	Integrated Carbon Observing System
NEON	National Ecological Observatory Network
ACRF	ARM Climate Research Facility
MPL-Net	Micro-Pulse Lidar Network
E-PROFILE	EUMETNET Program for European Scale Wind and Lidar Network
SPALNET	Spanish and Portuguese Aerosol Lidar Network
CANDAC	Canadian Network for the Detection of Atmospheric Change
ALC	Automatic lidars and ceilometers
SIRTA	Site Instrumental de Recherche par Télédétection Atmosphérique
<i>Defined Parameters</i>	
CBL-WS	Mean horizontal wind speed in the convective boundary layer retrieved from radiosonde profile
SHF	Sensible heat flux
SSWD	Downwelling solar radiation at the surface
z_i	ABL top height
z_i^{Max}	Daytime maximum z_i
LWCRF	Longwave cloud radiative forcing

[e.g., Denning et al., 2008; Haman et al., 2012]. In particular, z_i time series is considered a valuable data set for investigating convective boundary layer (CBL) processes (e.g., turbulence parameterization and scaling), for evaluating regional-scale atmospheric models, and for developing new parameterization schemes in numerical weather prediction models [e.g., Haefelin et al., 2012; Banks et al., 2015].

In recent years, several research infrastructures equipped with ground-based profilers like lidars and ceilometers were built up to understand the present state and predict future global element cycles: ICOS, NEON (National Ecological Observatory Network), ACRF (Atmospheric Radiation Measurement Program (ARM) Climate Research Facility), MPL-Net (Micro-Pulse Lidar Network), Canadian Network for the Detection of Atmospheric Change (CANDAC) differential absorption lidar (DIAL): CANDAC DIAL, EARLINET (European Aerosol Research Lidar Network), E-PROFILE (EUMETNET Program for European Scale Wind and Lidar Network), SPALNET (Spanish and Portuguese Aerosol Lidar Network), ALC (Automatic Lidars and Ceilometers) network, etc., [e.g., Milroy et al., 2012; Paris et al., 2014; Haefelin et al., 2012]. Table 1 summarizes the list of the acronyms used in this study.

Significant research initiatives were made in the last few decades to use long-term lidar-based investigations for monitoring optical properties of aerosol particles over different sites around the world [e.g., Matthias and Bösenberg, 2002; Pedrós et al., 2010; Pal and Devara, 2012; Kafle and Coulter, 2013; Amiridis et al., 2015]. However, studies on the z_i climatology based on multiyear lidar measurements have received little attention, partly for lack of continuous observations. In particular, routine, long-term, and high-resolution lidar-derived z_i time series were difficult to achieve until the very recent advancement in the automated lidar technology [e.g., De Tomasi and Perrone, 2006; van der Kamp and McKendry, 2010; Yang et al., 2013; Lewis et al., 2013; Ketterer et al., 2014; Pal, 2014].

Long-term lidar (or ceilometer) observations have been used, so far, to (1) demonstrate the feasibility of applying newly developed z_i retrieval algorithms [e.g., Chen et al., 2001; Baars et al., 2008; Granados-Muñoz et al., 2012; Di Giuseppe et al., 2012; Haman et al., 2012; Pal et al., 2013; Luo et al., 2014] and compare with model simulations [e.g., He et al., 2006; Denning et al., 2008; Collaud Coen et al., 2014; Korhonen et al., 2014], (2) compare results obtained from different data sets [e.g., Sawyer and Li, 2013], and (3) assess the

potential of ground-based lidars and ceilometers for long-term z_i monitoring [e.g., Pal *et al.*, 2013; Schween *et al.*, 2014]. However, most of these studies are based on 1 year observations so that interannual variability in z_i and growth rate was not reported. Thus, a comprehensive evaluation of the impact of near-surface meteorological conditions on diurnal, seasonal, interannual z_i variability remained difficult to perform, however, because long-term continuous measurements of z_i and growth rate are greatly needed.

This work benefits from the recent progress in the use of ground-based automated profilers for continuous unattended monitoring of z_i at SIRTA (Site Instrumental de Recherche par Télédétection Atmosphérique), a French national atmospheric observatory dedicated to cloud, aerosol, and ABL research, located near Paris, France. The key aim of this paper is twofold: (1) detailed investigation of the lidar-based z_i climatology focusing on diurnal, seasonal, and interannual timescales and (2) examination of several observational aspects of land-atmosphere coupling, and finally provides physical insights into the meteorological controls (e.g., downwelling solar radiation at the surface (SSWD), soil moisture, sensible heat flux (SHF), mean horizontal wind speed in the CBL (CBL-WS), and cloud cover) on ABL development, growth rate, and ABL growth phase over land.

2. Site, Instrumentations, Data Sets, and Methods

2.1. Experimental Site and Instrumentations

SIRTA, the measurement site for this study, is located in Palaiseau (2.208°E, 48.713°N, 160 m above sea level), ~20 km south of Paris on the Saclay plateau in a suburban environment. SIRTA is situated in the flat Parisian plain, surrounded by villages, agricultural fields, and some major roads connecting the suburban areas with the city of Paris. A large suite of state-of-the-art active and passive remote sensing instruments is operational at SIRTA since 2002 [e.g., Haeffelin *et al.*, 2012; Pal *et al.*, 2012].

A vertically pointing aerosol backscatter lidar (ALS-450, manufactured by Leosphere, France) was operated at SIRTA between 2008 and 2013. We used high-resolution (10 s and 15 m) profiles of aerosol backscatter to derive z_i . At SIRTA, a unified multiparameter data set (called SIRTA Re-OBS) was developed based on measurements of over 40 atmospheric and ground physical parameters. The data set covers the period from 2002 until present (see Cheruy *et al.* [2013] and Chiriac *et al.* [2014] for further details).

2.2. ABL Parameters and Analysis Approach

We investigate three key parameters of ABL diurnal cycle: daytime maximum z_i denoted as z_i^{Max} , z_i growth rate, and ABL growth duration. For instance, we choose z_i^{Max} for two main reasons: (1) previous studies using lidar measurements at SIRTA provided evidence that the z_i^{Max} coincide well with the elevated potential temperature (θ) inversion level obtained from the nearby radiosonde profiles at Trappes [e.g., Haeffelin *et al.*, 2012; Pal *et al.*, 2013] and (2), in general, on diurnal timescale, z_i^{Max} defines the “volume of the box” within which vertical mixing of trace gases and pollutants takes place [e.g., Yi *et al.*, 2001; Pal, 2014].

The growth rate determines the entrainment of free atmosphere (FA) air into the ABL [e.g., Stull, 1988] driven by varying land surface and FA conditions. Previously, several researchers illustrated that during the morning transition period when the CBL grows through the overlying residual layer (RL), entrainment velocity (w_e) can be quite high (up to 1.5 m s^{-1}) after that slower growth rate continues due to the entrainment from the FA [e.g., Nilsson *et al.*, 2001; Pal *et al.*, 2012]. In general, a large increase of the entrainment buoyancy flux occurs when the RL is incorporated into the growing CBL generating a sharp increase in the z_i [e.g., Conzemius and Fedorovich, 2006; Vilà-Guerau de Arellano *et al.*, 2009, 2011; Pal *et al.*, 2010; Janssen *et al.*, 2012]. Using observations and results from large-eddy simulation (LES), Blay-Carreras *et al.* [2014] illustrated that due to the presence of RL, growth rate becomes 2–3 times higher than for the regime with no RL above the stable boundary layer (SBL).

2.2.1. Determination of ABL Top Height (z_i)

Morille *et al.* [2007] developed an approach to determine locations of key aerosol vertical gradients derived from quality-controlled aerosol lidar observations. The method was further refined to account for two-dimensional aerosol gradients (STRAT-2D) [Haeffelin *et al.*, 2012] based on temporal and spatial resolutions of 30 s and 15 m, respectively. A new autonomous attribution technique to determine z_i (STRAT+) was developed at SIRTA by Pal *et al.* [2013]. It combines lidar-derived profiles of variance of relative

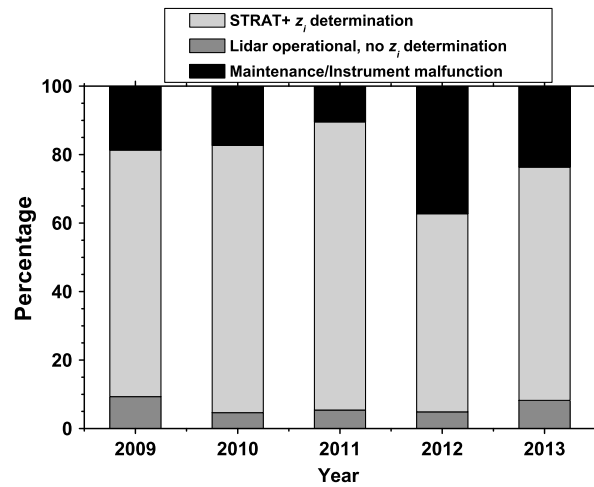


Figure 1. Data coverage of lidar measurement (in %) during 2009–2013. The black portions of the stack bars indicate the gaps (no data) due to maintenance and instrumental malfunction. The grey bars include the time when lidar data sets were available, but STRAT+ algorithm was not successful due to missing data from micrometeorological instruments, poor lidar data quality due to rain, and lidar signal degradation; light grey bar indicates the amount of time when z_i retrieval using STRAT+ algorithm was possible. Number of days when lidar measurements were available varies in different years (2009: 296, 2010: 301, 2011: 326, 2012: 228, and 2013: 232).

particle backscatter, STRAT-derived aerosol layers, and micrometeorological measurements near ground and, finally, allows near-real-time z_i determination at a temporal resolution of 10 min.

2.2.2. ABL Depth Growth Rate

The z_i growth rate is constrained by the inversion strength mainly via two phases: (1) at the early stage of CBL growth by the shallow nocturnal inversion close to the surface and (2) later in the day when growing CBL reaches the quasi-stationary z_i in the presence of synoptic high pressure [e.g., Stull, 1988; Blay-Carreras et al., 2014]. On a daily basis, we considered the z_i values for the morning transition period between the time of crossover (t_1) after sunrise and the time in the afternoon (t_2) when $0.9z_i^{Max}$ (i.e., 90% value of the z_i^{Max}) is reached. Finally, we determined the growth rate by fitting a linear regression line along the z_i observations between times t_1 and t_2 ; corresponding gradient yields the growth rate [e.g., Baars et al., 2008; Pal et al., 2013; Schween et al., 2014].

2.2.3. ABL Growth Duration

In general, the growing phase of ABL diurnal cycle refers to the period between the times of crossover of SHF (negative to positive, i.e., when SHF changes sign) and when z_i reaches a maximum value in the early or late afternoon. During this period, the nocturnal SBL which is usually shallow is rapidly eroded as the CBL grows. Often, growing CBL regime consists of two closely related phases: (1) formation of a shallow CBL after the nocturnal boundary layer (NBL) is eroded in the morning and (2) a rapidly growing CBL that will reach a quasi-stationary height, higher than that of the shallow CBL [e.g., Stull, 1988; Pal et al., 2015]. Following Yi et al. [2001], we investigated the time required for the z_i to reach its maximum value from the time of ABL onset. For each day, we estimated the interval between the crossover after sunrise and the time when CBL reaches its peak value in the late afternoon.

3. Diurnal, Seasonal, and Interannual Variability of ABL Parameters

The lidar data set over the period 2009–2013 is 76% complete as there are occasional gaps due to miscellaneous system malfunctions, maintenance, and other data unavailability. Figure 1 displays the detailed information about the data availability and the retrieval of z_i using STRAT+ algorithm. Because of intermittent instrument failures, some half-hourly data were missing from the ancillary products (e.g., SHF), and so the STRAT+ algorithm needed to take such missing values into account. While there are very large gaps during the autumn in 2012, the other seasons are sampled reasonably well.

3.1. Diurnal Cycle of z_i

In the following, we present a brief overview of the z_i time series obtained for the period between 2009 and 2013. To do this, we analyzed monthly-mean z_i diurnal cycles during different years which helped to illustrate the features of the development and maintenance of z_i including diurnal, seasonal, and interannual variability (Figure 2). The 5 year average monthly-mean composite of z_i illustrates the global means of z_i on both diurnal and seasonal timescales. The pseudocolored composites illustrate diurnal asymmetry, morning CBL development, afternoon z_i^{Max} , and seasonal variability. The main features of diurnal (seasonal) variability in z_i are higher z_i in daytime (summer and spring) compared to z_i in nighttime (autumn and winter). Overall, both the diurnal and seasonal variability in the z_i followed the SSWD cycle measured at the site. For instance,

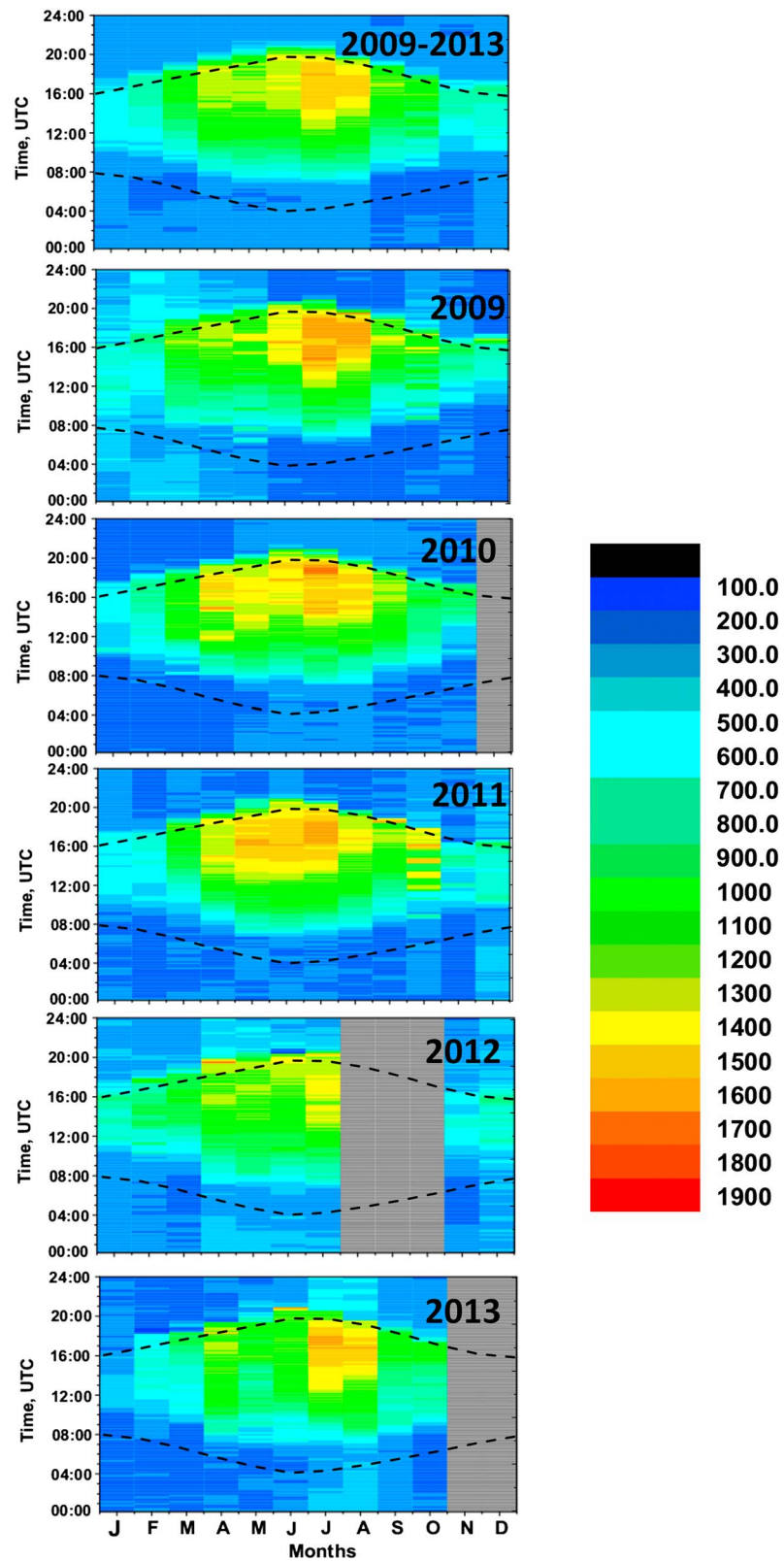


Figure 2. Pseudocolored composites of the monthly-mean diurnal cycles of ABL depths illustrating variability in the diurnal and seasonal z_i cycles over the SIRTA site during 2009–2013. Vertically-aligned color bar on the right denotes the z_i values. Average (mean) z_i for each 1 h period in the day, and for each month of the year (color scale, meters above ground level (agl)) determined during different years over SIRTA using the STRAT+ method. Vertical grey bars indicate data gaps in 2010 and 2012.

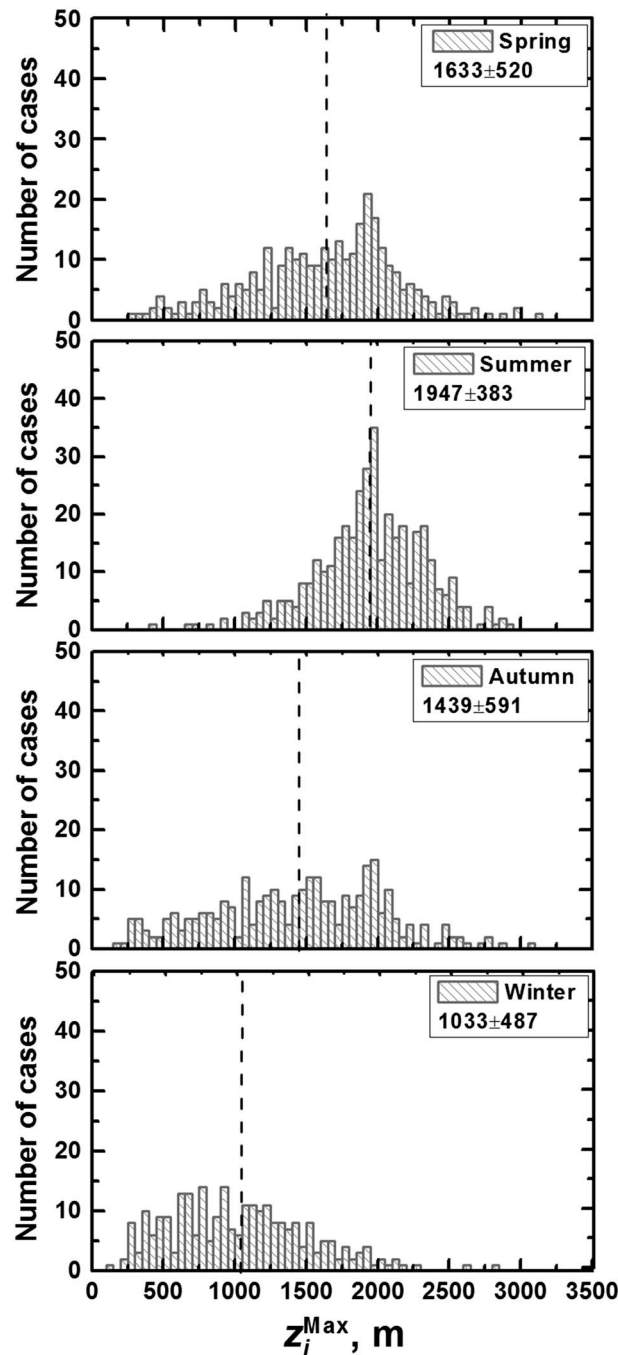


Figure 3. Histogram showing the frequency distribution of daily afternoon maximum CBL heights (z_i^{Max}) for all measurements (2009–2013) as a function of seasons for bins of every 50 m interval. Dashed line on each panel marks the seasonal mean of z_i^{Max} . Median values of the distributions in spring (1695 m) and summer (1957 m) are higher than in autumn (1493 m) and winter (985 m). Seasonal mean values with corresponding standard deviations are also shown in the top right corner of each panel.

(Figure 3). Both summer and spring distributions showed negative skewness confirming high values being more frequent than low ones in those seasons unlike in autumn and winter for which z_i^{Max} distributions yielded positive skewness. Our results also suggest that the cases with $z_i^{\text{Max}} > 1500$ m in summer (spring)

for all years, the months of April, May, June, and July have the longest and deepest z_i diel cycle.

The monthly-mean diurnal cycles for each season, December–February (DJF) (winter), March–May (MAM) (spring), June–August (JJA) (summer), and September–November (SON) (autumn), illustrate that overall winter (summer) has the lowest (highest) daytime ABL peak. As a note, due to 3 months of gaps in the lidar measurements in 2012, the results related to the z_i seasonal variability for the autumn of 2012 are not statistically significant. The z_i mean diurnal cycles suggests that the z_i during the afternoon were quasi-stationary without any significant growths for more than 3 h.

3.2. Atmospheric Boundary Layer Features

3.2.1. Daytime Maximum z_i

Using frequency distribution analyses of daily z_i^{Max} , we investigated the boundary layer regimes and relevant z_i variability for the entire period. Standardized z_i^{Max} frequencies for four seasons were considered using a z_i^{Max} bin size of 50 m (Figure 3). The summer z_i^{Max} frequency follows well-defined “bell-shaped” curve (typical of a Gaussian) ranging from 500 to 3000 m with most frequency occurring at ~1960 m (~40 samples). In contrast, the autumn z_i^{Max} frequency is found with a broad and flat distribution with a wider z_i^{Max} range from 200 to 2500 m with a median at 1493 m. In winter, a relatively higher (lower) number of cases were observed for smaller (larger) z_i^{Max} bins. Additionally, the winter frequency distribution was mainly characterized with higher number of cases with shallow boundary layer depth and similar though not identical to autumn distribution ranging from 100 to 2100 m with a median at 985 m. Nevertheless, the frequency distributions presented yield a clear seasonal variability with the highest (lowest) mean of z_i^{Max} of 1947 m (1033 m) in summer (winter).

The frequency distributions of z_i^{Max} differ significantly among different seasons as indicated by the standard deviation values

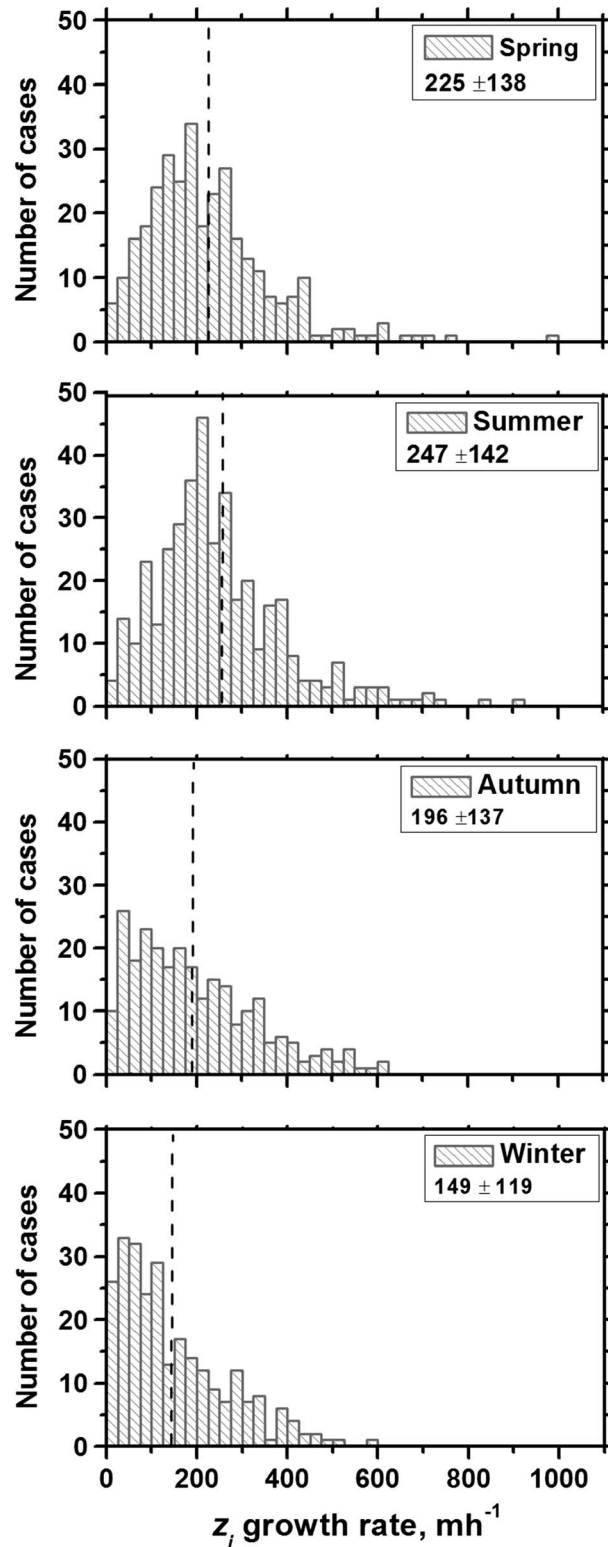


Figure 4. Same as Figure 3 but for the z_i growth rates illustrating seasonal variability. A bin size of 25 m h^{-1} is used. The dashed line on each panel marks the seasonal mean growth rate. The distributions in spring and summer show a nearly bell-shaped curve with a peak around 195 m h^{-1} and 220 m h^{-1} , respectively. The median values for autumn and winter are 169 and 112 m h^{-1} , respectively.

are 89% (63%), illustrating a clear tendency for deeper CBL in summer than in spring (Figure 3). These results are similar to the recently reported measures of z_i variability in different seasons over other European sites [e.g., Baars et al., 2008; Pal et al., 2010; Granados-Muñoz et al., 2012; Zhang et al., 2013]. We also found larger day-to-day z_i^{Max} variability during autumn and spring than in summer and winter. A large interannual variability in z_i^{Max} was also observed during spring and autumn. Yang et al. [2013] also found similar z_i^{Max} distributions for different seasons for Hong Kong based on 6.5 years of lidar measurements.

3.2.2. Growth Rate of z_i

The frequency distribution analyses for the growth rate (Figure 4) reveal annual cycles similar to those of z_i^{Max} with higher mean growth rates in summer (247 m h^{-1}) than in winter (149 m h^{-1}). Moderate number of cases with very high growth rate ($>400 \text{ m h}^{-1}$) were also observed, however, only predominantly in summer and spring. The spring and summer frequency distributions yielded a quasi-Gaussian shape with symmetric and unimodal distributions as was confirmed with their kurtosis (a measure of the “peakedness”) values of around 3. In contrast, autumn observations showed nearly flat distributions with positive skewness confirming higher number of cases with relatively lower growth rates ($25\text{--}100 \text{ m h}^{-1}$). The standard deviation values for the four distributions also showed some seasonal variability with higher standard deviation in summer (142 m h^{-1}) than in winter (119 m h^{-1}) which most likely illustrates relatively higher day-to-day variability in the ABL governing factors like near-surface forcing (e.g., SHF), changes in FA lapse rate, and the presence of RLs above the NBL, in summer than in winter.

Most of the differences in the shape, width, and median values in the growth rate distributions could be attributed to the day-to-day as well as interannual variability in the CBL regimes during the study period. Following box-and-whisker analyses of the growth rates, we also found that the growth rate attained maximum

Table 2. A Brief Overview of the Reported z_i Growth Rates Over Land Surface Based On Ground-Based Lidar Observations Over Some Selected Sites Around the World

List of References (Chronological Order)	Experimental Site or Region	Length of Time Series or Type of the Study	Reported z_i Growth Rate ($m\ h^{-1}$)
Yi et al. [2001]	Northern Wisconsin, USA	8 months	250–300 with seasonal variability
Chen et al. [2001]	Tsukuba, Japan	1 year	30–100 with seasonal variability
Pino et al. [2004]	Barcelona, Spain	Case study	150
Baars et al. [2008]	Leipzig, Germany	1 year	100–300 with seasonal variability
Denning et al. [2008]	Northern Wisconsin, USA	1 year	275
Pal et al. [2010]	Stuttgart, Germany	Case study	200
van der Kamp and McKendry [2010]	Vancouver, southwest coast of BC, Canada	2 years	50–110 with seasonal variability
Pal et al. [2012]	Paris and suburban region, France	Case study	100–250 with seasonal variability
Yang et al. [2013]	Yuen Long, Hong Kong, China	6.5 years	50–100 with seasonal variability
Lewis et al. [2013]	Greenbelt, Maryland, USA	7 years	100–150 with seasonal variability
Schween et al. [2014]	Jülich, Germany	1 year	50–130 with seasonal variability
Korhonen et al. [2014]	Johannesburg, South Africa	1 year	100–300 with seasonal variability
Collaud Coen et al. [2014]	Payerne, Switzerland	2 years	150–250 with seasonal variability
Pichelli et al. [2014]	Rome, Italy	Case study	250–275
Pal et al. [2015]	Trainou, France	1 year	75–200 with seasonal variability
This study	Palaiseau near Paris, France	5 years	150–225 with seasonal variability

of around $400\text{--}600\ m\ h^{-1}$ in all the years except in 2013. The observed turbulent mixing parameters were up to 2–3 times weaker in 2013 compared to the other years which most probably caused this interannual variability. The year 2013 was a very particular one among other years, with a large deficit in cloud free situations, and excess of rain from December to June, while July and August were rather close to “normal” summer months. In 2013, October was the rainiest month (monthly accumulated precipitation of 108.4 mm). Based on daytime maximum temperature climatology, February was the coldest month in

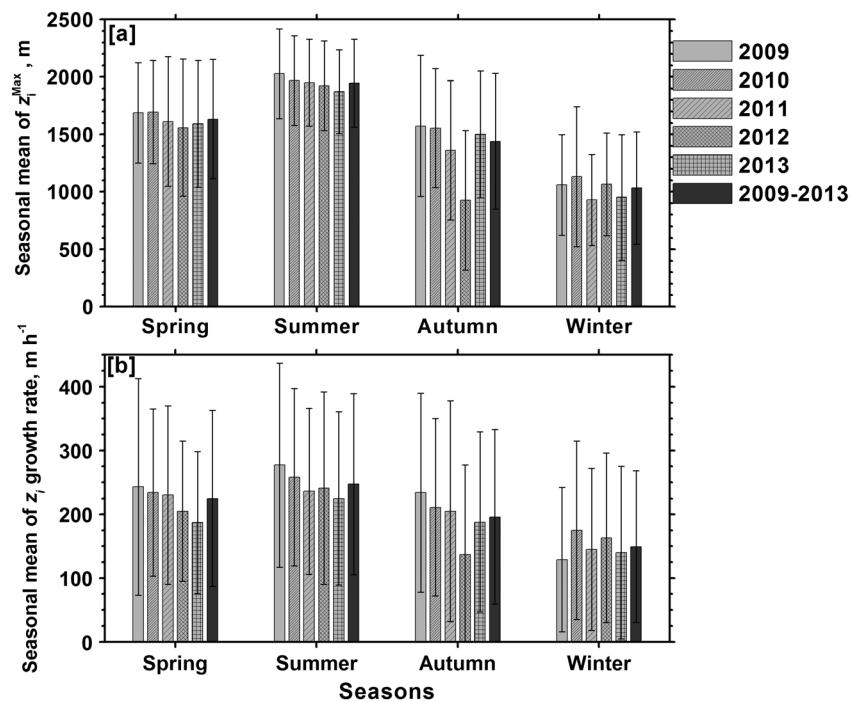


Figure 5. A brief overview of the seasonal and the interannual variability in the observed (a) z_i^{Max} and (b) growth rate. The global mean values (i.e., averaged over 2009–2013) of both parameters are also shown. Seasonal mean values of both parameters for autumn 2012 and winter 2011 and 2013 are obtained with incomplete data coverage. Error bars represent 1 standard deviation values for both parameters.

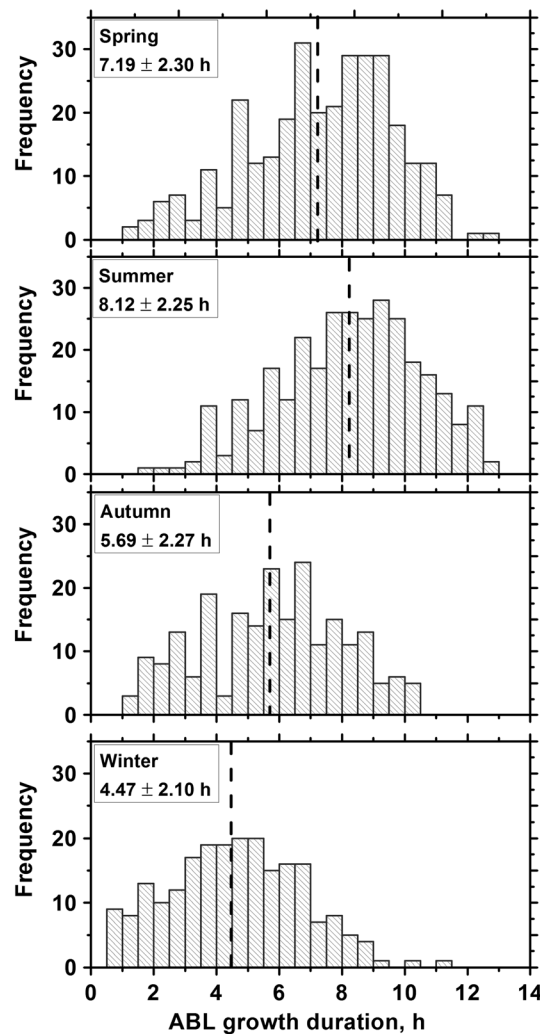


Figure 6. Same as Figure 3 but for the daily ABL growth duration (in h) illustrating seasonal variability in the growing phase of CBL. A bin size of 0.5 h is used for the analyses. Mean values of the distributions are shown by the dotted lines and with corresponding standard deviations in the upper left corner of each panel. Median values of the distributions in spring (7.50 h) and summer (8.33 h) are higher than in autumn (5.83 h) and winter (4.50 h).

sunrise and crossover as well as larger amount of SHF, CBL grows for a longer time in summer months than in winter months. In the summer months, it was observed quite often that the peak afternoon z_i were elevated till the time before sunset. We also carried out box-and-whisker analyses of the daily growth durations to investigate further the temporal variability (as was done for z_i^{Max}). Some interannual variability was found, in particular, during spring and autumn (not shown here). However, the histograms reveal wide distributions in all seasons (Figure 6) and without any significant seasonal variability in their standard deviation values (2.1–2.3 h).

We also found that the growing phase varies significantly from one day to the other even within a season as can be seen from their values lying between 2 and 10 h. The results presented here highlight the role of near-surface thermodynamics on growing CBL features and suggest a new parameter (i.e., growth duration) for evaluating the treatment of z_i and growth rate in atmospheric models, in particular, in analytical models and in LES. In the past, *Raupach and Finnigan* [1995] suggested that z_i variability often reflects a timescale equivalent to growth duration which could be many hours, perhaps 8 h or more by afternoon.

2013 (mean monthly average of 2.5°C). We also found that growth rate showed strongest inter-annual variability for autumn as was observed for z_i^{Max} .

The seasonal variability in the growth rates reported in this study is consistent with the other studies mentioned before. For instance, using lidar measurements over Leipzig, Germany, *Baars et al.* [2008] reported growth rates of 100 to 300 m h^{-1} most of the year, while *Pal et al.* [2014] reported slightly lower growth rates of about 150–200 m h^{-1} over a rural site in France. *Chen et al.* [2001], however, reported much lower growth rates of 30 to 100 m h^{-1} for a remote site (Tsukuba) in Japan. Table 2 summarizes some of the key findings on z_i growth rates over different sites around the world. While comparing the growth rates over different sites, it should be noted that growth rates largely depend on geographical location, predominant land use in the surrounding area (e.g., proximity to urban areas and agricultural areas or forests), cloudiness, and local climate [e.g., *Liu and Liang*, 2010; *Lewis et al.*, 2013]. A brief overview of the seasonal variability in the z_i^{Max} and growth rate during 2009–2013 is presented in Figure 5, which can serve as a basis for comparing these results with other midlatitude sites.

3.2.3. Growing Phase of ABL

We also performed frequency distribution analyses of daily ABL growth duration for four different seasons (Figure 6). On average, we found a clear seasonal pattern in the growth duration illustrating relatively longer time to reach the z_i^{Max} in summer (~8 h) than in winter (~4 h). Monotonic seasonal patterns were also observed for both $T_{\text{SHF}}^{\text{Crossover}}$ (i.e., the time of SHF crossover) and $T_{\text{CBL}}^{\text{Max}}$ (i.e., the time when z_i^{Max} is attained), however, in opposite phase: earlier $T_{\text{SHF}}^{\text{Crossover}}$ in summer than in winter and vice versa for $T_{\text{CBL}}^{\text{Max}}$ (not shown here). Thus, due to earlier

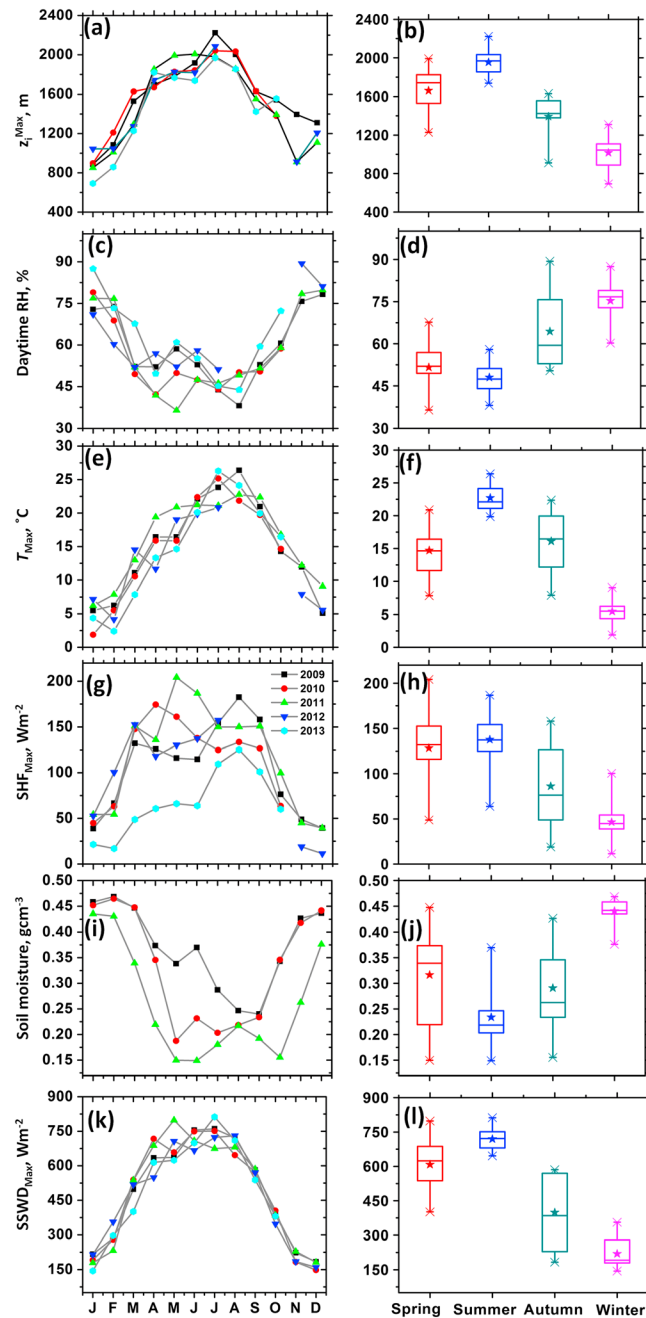


Figure 7. (a, c, e, g, i, and k) Time series of monthly-mean values of z_i^{Max} , RH_{Min} , T_{Max} , afternoon SHF_{Max} , q_{soil} , and $SSWD_{Max}$; panels from bottom to top illustrate the governing factors and mechanisms for the variability of z_i . Different colored symbols mark different years. (b, d, f, h, j, and l) Corresponding mean seasonal variability based on the monthly-mean values for the period between 2009 and 2013 via box-and-whisker analyses. In each box solid line indicates the median and the extent of boxes, 25th and 75th percentiles; whiskers represent the 10th/90th percentile markers. The central point is the mean value, and the external points are the maximum and minimum.

inspection reveals that afternoon soil moisture at all levels (-5 cm, -10 cm, and -20 cm) at the site shows a bimodal pattern during the year, with one maximum in winter and another one in early to late summer. It can also be seen that z_i^{Max} in 2009 occurs in July, corresponding with maximum SHF and maximum

4. Dependence of z_i on Near-Surface Meteorological Parameters

4.1. Seasonal Variability

This section presents different aspects of near-surface forcing on z_i variability on both seasonal and interannual timescales. We consider two types of near-surface micrometeorological and meteorological parameters: (1) variables that directly influence z_i evolution like SHF, SSWD, soil moisture, and CBL-WS and (2) variables which cotemporally vary with z_i like near-surface temperature. The combined time series of monthly means of daily maximum SSWD ($W m^{-2}$), midafternoon soil moisture ($g cm^{-3}$), SHF ($W m^{-2}$), near-surface temperature (T_{2m} , $^{\circ}C$), relative humidity (RH_{2m} , %), and z_i^{Max} are first considered (Figures 7a, 7c, 7e, 7g, 7i, and 7k). Additionally, to represent the seasonal cycle of these near-surface meteorological parameters, we performed box-and-whisker analyses (Figures 7b, 7d, 7f, 7h, 7j, and 7l). Clear seasonal variability can be observed for all parameters with cyclic behavior illustrating higher (lower) temperature, z_i , and SSWD in summer (winter) months. Additionally, the annual cycle is also evident for SHF, with mean daily (24 h) SHF reaching a maximum in spring and summer and a minimum in winter months. A clear seasonal cycle was also found in the soil moisture parameter: drier soil in summer and wet soil in winter with highest variability in spring (Figure 7j).

Overall, there is remarkably good agreement across the three data sets ($SSWD$, T_{2m} and z_i), which capture seasonal similarities. However, both midday soil moisture and daytime minimum RH showed an opposite annual cycle that most likely occurred due to higher amount of soil moisture due to precipitations in winter than in summer months at SIRTA. The RH seasonal cycle is also driven by temperature. A close

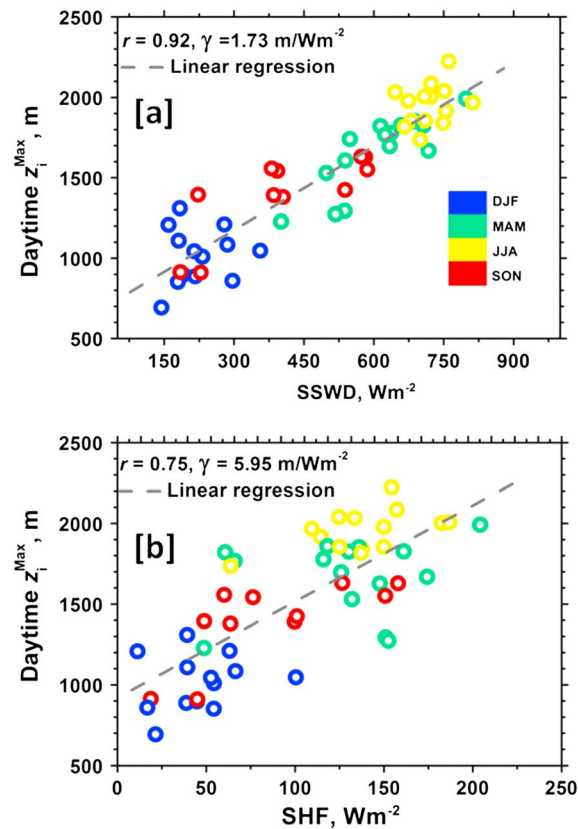


Figure 8. Scatterplots and regression analysis between monthly-mean values of z_i^{Max} and (a) SSWD_{max} and (b) SHF for the entire measurement period. The linear regression (dashed grey line) and corresponding correlation coefficient and gradient values (γ , m/Wm^{-2}) are shown in each panel. The colors of the circles correspond to different seasons (see the color bar in Figure 8a).

SSWD, which occurs in June. But, in 2011, this correspondence does not hold true, which could be attributed to the surface energy balance in those months.

4.1.1. Dependence of z_i on SSWD and SHF on Seasonal Scale

SSWD is one of the key driving factors governing the temporal variation of z_i on both diurnal and seasonal timescales. Since SSWD largely varies due to solar zenith angle, cloud cover, cloud optical depth, and amount of aerosols present in the atmosphere, significant seasonal variability as well as interannual variability could be observed. Consequently, this variability impacts the z_i variability. Thus, we find it interesting to investigate the relationship between (1) the SSWD and z_i and (2) the SHF and z_i (Figure 8). The scatterplots illustrate the regression analyses for the 5 year period. The colors of the circles in each panel mark four different seasons. The relationship between z_i and SHF ($r=0.75$) is not fully linear, in particular, during summer when the z_i values are highest, while the SHF values remain in the same range as is found for spring month. These results are similar to the findings reported by other researchers in the past [e.g., Bianco et al., 2011; Pal et al., 2012]. More recently, Molod et al. [2015] while investigating spatial z_i variability using NOAA wind profiler network data also found a general pattern indicating similar dependence of z_i on surface temperature and moisture. In their study, they also reported higher (lower) z_i for warmer and drier (cooler and moister) areas.

It should be, however, noted that since the results presented in this study and in the aforementioned studies are based on the linear regression approach while the impact of ensemble of atmospheric parameters on boundary layer evolution is not strictly linear, future research should definitely consider applications of other advanced statistical approaches like multiregression analyses and factor separation approaches to explore further the dependence of z_i variability on both near-surface meteorological conditions and free tropospheric processes.

It could be clearly seen that winter z_i is mainly < 1200 m (90th percentile), summer $z_i > 1800$ m (90th percentile), while spring and autumn z_i are intermediate, with spring z_i higher than fall z_i . Monthly-mean SSWD vary from ~ 150 (winter) to 850 W m^{-2} (summer) indicating clear seasonal variability. Being SSWD is a key driver of surface heating, and of convection, the seasonal variations of SSWD and z_i are correlated with good linear relationship ($r=0.92$). Monthly-mean SHFs vary from 20 (winter) to 200 (summer) W m^{-2} . Seasonal separation is not as clear in particular for spring and summer. Spring and summer SHFs are very close (ranging from 100 to 200 W m^{-2}). Fall SHF ranges from 20 to 150 W m^{-2} , while winter SHF ranges from 20 to 100 W m^{-2} . So in spite of highest SSWD in summer, SHF reaches a plateau between 150 and 200 W m^{-2} . The linearity between SHF and z_i is not well developed ($r=0.75$ as appeared in the scatters). In summer, in spite of limited SHF, z_i^{Max} reach higher altitudes than in spring, which could be attributed to the other sources that also influences z_i^{Max} such as advection of different air masses from adjacent urban areas, presence of clouds, and temporal shift in the times of z_i^{Max} and SHF_{Max} . Yi et al. [2001] while discussing the implications for SHF-based relationship for z_i variability found that often CBL grows for more than 3 h even after SHF reached its daytime peak value.

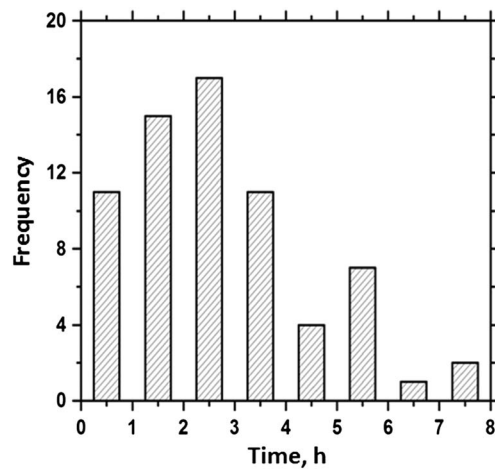


Figure 9. Frequency distribution of the number of hours from the time of maximum SHF to the time of the maximum CBL z_i . Data sets obtained between February and September in 2011 were used here.

tely. This variability in time of z_i^{Max} and SHF_{Max} is most certainly responsible for part of the nonlinear behavior observed in Figure 8b.

We also argue that although the SHF is one of the important surface-based drivers of z_i , it is not the sole driver generating the diurnal and day-to-day variability in z_i . Vilà-Guerau de Arellano *et al.* [2009, 2011] investigated the roles of CBL and RL wind speed in modulating CBL growth in the morning. Subsidence, although a synoptic scale phenomenon, plays an important role in determining the z_i^{Max} . Other potential attributes may include the effects of RL, and horizontal advection. Additionally, it is a well established fact that the error in measuring the SHF is larger than that for the SSWD, due to the propagation of errors from eddy covariance measurements.

4.1.2. Variability in z_i and Relevant Surface Forcing in Two Contrasting Years

Pseudocolored composites of monthly-mean diurnal cycles of SSWD, SHF, near-surface temperature, and z_i for 2009 and 2011 are considered to highlight both seasonal and diurnal variation together in each parameter (Figure 10). Daily sunrise and sunset times are also indicated to illustrate the CBL onset during morning transition period and the NBL during evening transition period in different months. Similar analyses were performed for other years; however, we discuss only the results obtained for 2009 and 2011 in detail due to (1) two contrasting meteorological regimes present in these two years and (2) availability of largest amount of high-quality lidar data sets without major gaps in the time series.

The differences in z_i and its evolution during different seasons can be observed in both years. However, the four parameters exhibit strong contrasts between 2009 and 2011 (Figure 10). It was also found before that the z_i seasonal variability in 2009 is similar to the 5 year mean seasonal cycle of z_i (Figure 5). Spring SSWD values are significantly higher in 2011 than in 2009. In the same season, we find the longest warm spell in 2011 from March to April, constituting 24 consecutive days with higher daytime temperature compared to the monthly-mean daytime temperature. In addition, the longest dry spell was in April 2011, constituting 25 consecutive days with no measured precipitation. Positive anomalies from the mean SSWD are attributed to a deficit in cloud cover. An exceptionally hot and dry spring in 2011 was observed in mainland France mainly due to persistent influence of anticyclonic conditions [e.g., Chiriaco *et al.*, 2014]. We also noted that soil moisture concentrations were significantly lower in those months in 2011 than in 2009 (Figure 7). Higher than normal SSWD associated with a dry soil yielded much higher SHF in spring 2011 than in spring 2009. Temperatures in April–May 2011 are similar to those of June–July (Figure 7). While spring z_i values in 2011 are higher than in 2009, summer months reveal comparable values which could be attributed to the frequent precipitation in summer 2011. The recorded monthly accumulated precipitations for the months of June, July, and August in 2011 (2009) were 81.63 (42.44) mm, 58.83 (42.61) mm, and 64.03 (18.20) mm, respectively. Thus, the accumulated summer precipitation in 2011 (204.5 mm) was significantly higher than in 2009 (103.3 mm).

The variability observed in the time (in h) between the times of maximum SHF and the time when the z_i reaches its maximum is further analyzed (Figure 9). We considered the measurements obtained on the days without extensive cloud covers and precipitation. For demonstration purpose, we investigated the measurements obtained between February and September in 2011 only. For a particular day, we considered the measurements for the period when CBL was growing. We found that 2 h is the dominant time lag between the time when SHF reaches its maximum and the time after which no further z_i growth is observed. However, for some cases, the CBL continues to grow for more than 5 h after the time when the SHF reaches maximum value. Therefore, our results suggest that although the growth rate significantly slows down after SHF reaches maximum depending on weather conditions and season, z_i does not stop growing comple-

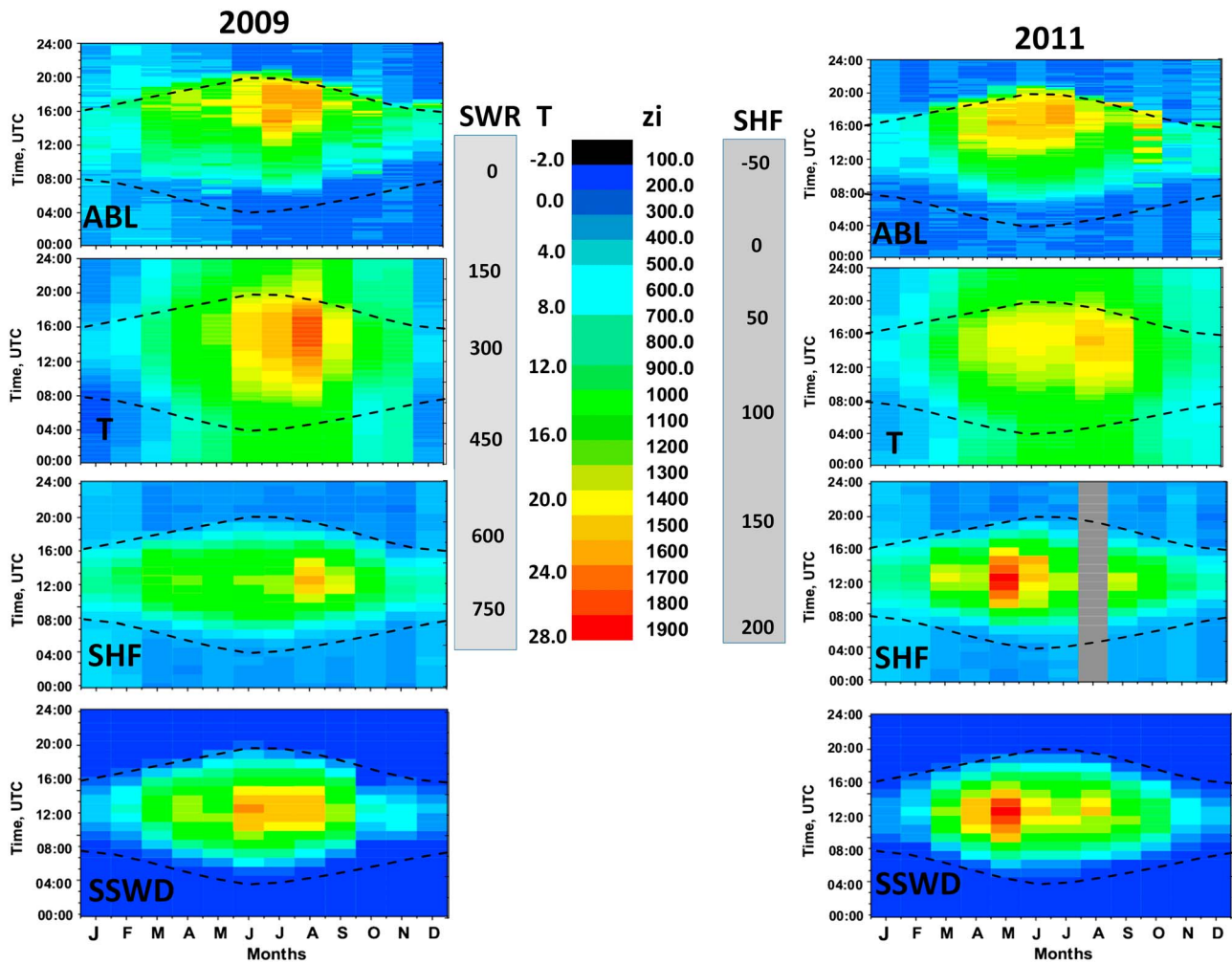


Figure 10. Monthly-mean diurnal cycle composites of SSWD ($W m^{-2}$), SHF ($W m^{-2}$), near-surface temperature (in $^{\circ}C$), and z_i (meters above ground level, agl) for (left column) 2009 and (right column) 2011. See different color bar scale limits for four different variables. Sunrise and sunset times during different months are overlaid as dashed black lines on each panel to illustrate the ABL regimes during morning and evening transitions. All the parameters experience strong diurnal and seasonal variability. Vertical grey bar indicates data gap in the SHF variability in 2011.

As a note, the correlation between SHF and the CBL-related parameters (z_i and growth rate) was not found to be very strong which could be mainly attributed to fact that CBL development is not only regulated by SHF but also by other physical mechanisms like variability in the horizontal convergence, vertical pressure velocity, subsidence, and FA lapse rate [e.g., Stull, 1988]. We suggest that future research effort focusing on multiregression analyses using both observational and modeling approaches is required.

Using collocated lidar and meteorological measurements at SIRTA, the features of the daytime z_i evolutions during four seasons are analyzed in detail which provides a good basis for z_i climatology over a suburban site in the mid-latitude. However, it should be noted that 2011 being a year characterized with atypical meteorological regimes for the site, both opportunities and challenges are involved while considering model-based simulation and/or evaluations of numerical models for investigating z_i variability in 2011; thus, should be performed with caution.

4.2. Interannual Variability

To further investigate the interannual variability in the observed z_i and the near-surface meteorological parameters, the seasonal variability is removed from the monthly-mean values. Deseasonalized monthly-mean anomalies are derived for each variable. The anomalies of each parameter for the observation period are derived as

$$A'_k = A^k - \bar{A}^k$$

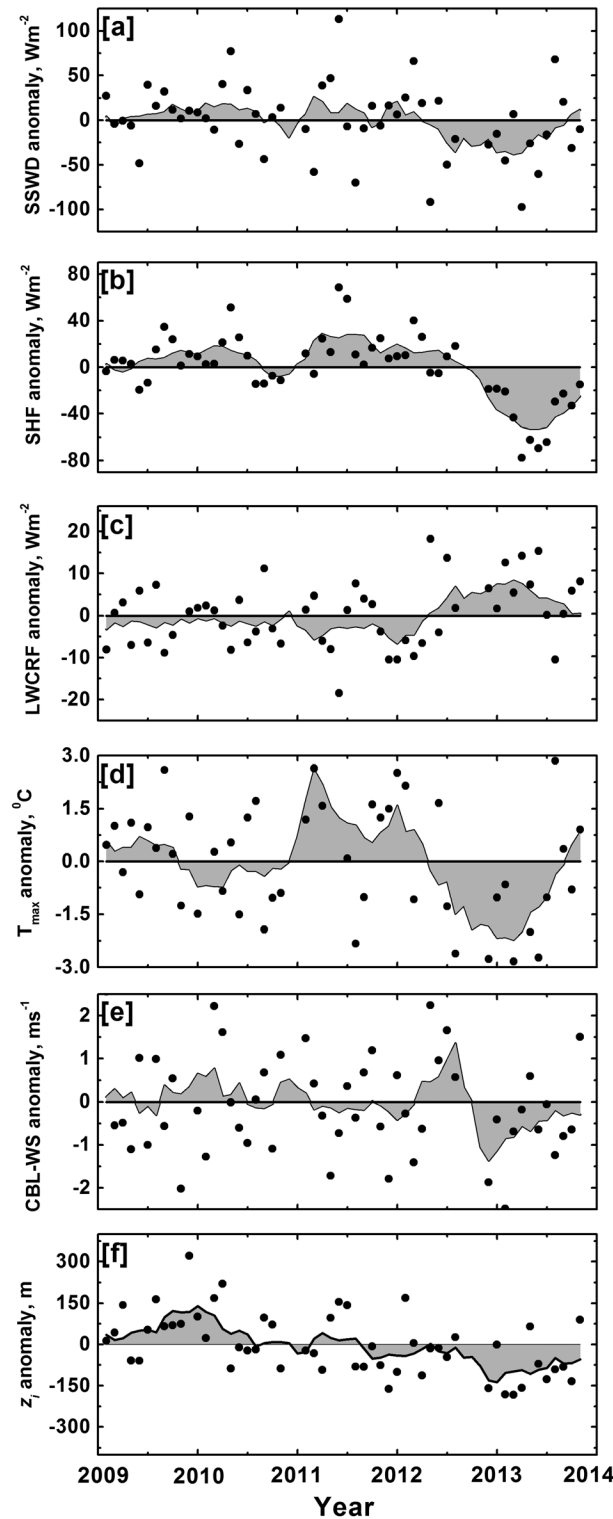


Figure 11. Time series of anomalies of monthly-mean values of daytime maximum (a) SSWD, (b) SHF, (c) LWCRF, (d) T_{Max} , (e) CBL-WS, and (f) z_i . Six month running average for each time series is overlaid.

further confirms the fact that the z_i variability on the interannual timescale is not directly governed by SSWD. Similarly, monthly-mean anomalies of z_i and SHF were correlated yielding a better correlation than with SSWD (r of 0.39, not shown here). Since SHF is one of the key drivers of z_i variability, we found it reasonable

where A is the parameter of interest (e.g., monthly-mean values of daytime maxima of SSWD, SHF, LWCRF (longwave cloud radiative forcing), T_{Max} , CBL-WS, and z_i), k denotes the month of a year (e.g., January and February), and the over bar indicates the global mean values (2009–2013) in a particular month. Subtracting the 5 year monthly-mean value from the monthly-mean value of individual year yields deseasonalized monthly-mean anomalies A' . Five years is likely not enough to construct a fully reproducible seasonal cycle, and hence, the resulting anomalies are not entirely deseasonalized. However, this method allows us to highlight for each month if the value is below (negative anomaly) or above (positive anomaly) the 5 year mean value. The LWCRF was calculated by subtracting clear sky surface downwelling longwave radiation from the observed surface downwelling longwave radiation.

The deseasonalized anomalies for each parameter illustrate their interannual variability (Figure 11). For instance, toward the end of the period, from mid-2012 to end of 2013, there is a lasting negative SSWD anomaly (more clouds as confirmed by the positive LWCRF anomaly), negative temperature anomaly, negative SHF anomaly, and a resulting negative z_i anomaly. Thus, cloudiness could be considered as an important driver for the observed variability. For instance, Figure 5 clearly illustrated that the wintertime has a higher variability due to higher cloudiness typically occurring during the winter over the site. Also, during summer of 2011, a positive SSWD and SHF anomaly period corresponds well to positive z_i and positive T_{Max} anomalies. The overlaid 6 month running mean curves for each parameter also illustrate the interannual variability.

Linear regression analyses between monthly-mean values SSWD and z_i showed high correlation between them as both parameters follow a similar seasonal pattern. However, while correlating monthly-mean anomalies of z_i and SSWD, we found no significant correlation (r of 0.22, not shown here) which

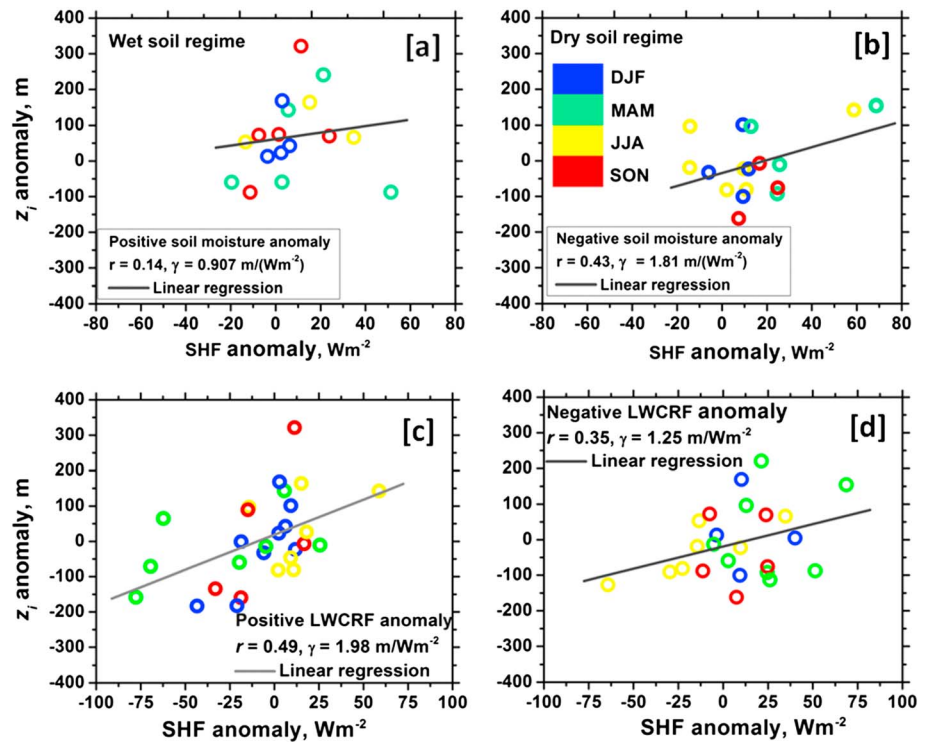


Figure 12. Conditional sampling and linear regression analyses between anomalies of monthly-mean values of z_i^{Max} and daytime maximum SHF with (a) positive and (b) negative anomalies of soil moisture as constraint, and with (c) positive and (d) negative LWCRF anomalies as constraint, and corresponding r and γ (in m/Wm^{-2}) values are also shown.

to apply conditional sampling analyses to obtain detailed understanding on the impact of this surface forcing on z_i variability so that contributions of other factors like soil moisture, cloud cover, and CBL-WS could be found.

4.3. Conditional Sampling Analyses for Determining z_i Dependence on SHF

We explore further the relationship between the anomalies of z_i and SHF to illustrate some of the important physical mechanisms and land surface processes governing z_i variability. Additionally, linear regression analysis presented in the previous section suggested that the SHF variability forces the ABL and its evolution differently during different seasons and years. To investigate further the impact of SHF on z_i , we use three different conditional sampling analyses based on the relationship between anomalies of SHF and z_i with the anomalies of (1) soil moisture, (2) LWCRF, and (3) CBL-WS as constraints.

4.3.1. Effect of Soil Moisture

Soil moisture plays an important role in surface energy balance via modulating thermal conductivity and hence the ground heat flux via separating total amount of heat flux into latent and sensible components and affects the surface albedo and transpiration by surface vegetation [Stull, 1988]. Higher amount of soil moisture helps reduce the surface heating and subsequent development of z_i as was previously demonstrated by Pan and Mahrt [1987].

We classified the soil moisture regimes into two broad categories: positive and negative soil moisture anomalies indicating wetter and drier than the 5 year monthly-mean soil regimes, respectively. Finally, the classification helps to find the dependence of z_i on SHF for these two broad classes of soil moisture regimes. The covariation between the anomalies of SHF and z_i for both regimes of soil moisture concentrations was performed (Figures 12a and 12b). The results based on linear regression and conditional sampling analyses suggest that the impact of SHF on z_i is more pronounced for dry soil regimes although for both cases z_i monotonously increases with increasing SHF.

Additionally, for dry regimes, increase in z_i was found to have a stronger dependence on SHF (γ of $1.81 m/W m^{-2}$) compared to the wet regimes (γ of $0.90 m/W m^{-2}$). In general, higher SHF with relatively drier soil regime

drives the ABL thermals to greater heights yielding higher z_i^{Max} . According to Figure 12b, this is a more valid assumption in summer than for other seasons. In contrast, during a relatively wet episode, a higher part of the net radiation is portioned into latent heat, with less SHF available to drive thermals in the ABL. The latent heat fluxes could have an indirect effect on z_i , as they characterize transfer of moisture from the soil to the CBL, which feeds CBL cloud formation, and subsequently z_i development. Therefore, in the presence of stronger latent heat fluxes, z_i development could be affected by other processes, hence affecting its correlation with SHF.

The results based on these conditional sampling analyses show that land surface processes are more coupled to the ABL evolution for drier soil conditions compared to the wet regimes. These results also suggest the influence of soil moisture on the development and triggering of CBL z_i variability in different atmospheric conditions in different seasons and could be a good basis for obtaining simple formulation of CBL over land for use in large-scale models.

4.3.2. Impact of Cloud Cover

In general, cloudiness affects the solar radiation reaching the Earth's surface and thus weakens convective mixing. We consider that on days when shallow cumulus clouds are initiated, presumably by thermal updrafts associated with surface sensible heating. While considering the annual cycle of cloud covers, we found that the relatively low z_i^{Max} in winter and autumn can also be attributed to increased cloudiness and therefore less heating from the surface. Surface radiation measurements are quite often used to assess the cloud fraction. LWCRF is mostly sensitive to low-altitude clouds, such as boundary layer clouds, because high-altitude clouds such as cirrus clouds do not have a significant signature in the downwelling longwave irradiance reaching the surface. LWCRF is also of interest as it is not affected by aerosols.

We performed conditional sampling analyses between SHF and z_i^{Max} anomalies for two scenarios considering LWCRF anomalies. For the cases with positive LWCRF anomalies, a higher correlation coefficient is obtained (r of 0.49 and γ of 1.98 m/W m^{-2}) compared to the cases with negative LWCRF anomalies (r of 0.35 and γ of 1.25 m/W m^{-2}) although the differences between the r is not significant. The gradient is stronger under positive LWCRF anomalies predominantly due to cases of negative SHF and z_i anomalies, occurring in fall, winter, and spring (Figure 12c). In summer, for scenarios with fewer clouds than the 5 year monthly-mean conditions, SHF and z_i anomalies are well correlated (Figure 12d). Negative (positive) SHF anomalies coincide with negative (positive) z_i anomalies. These conditions likely coincide with drier soil moisture as discussed in section 4.3.1, for which SHF has a predominant role in forcing the ABL development. Other seasons show much more scatter in SHF and z_i anomalies. We conceive that further empirical analyses are obviously required in particular to determine if the clouds are boundary layer clouds, or deep clouds decoupled from the boundary layer. The anomaly in LWCRF provides a straightforward estimate of an excess or deficit of cloud cover compared to a mean situation.

4.3.3. Effect of Horizontal Wind Speed in the CBL

Using the daily 12 UTC radiosonde-derived profiles of horizontal wind speed within the CBL (henceforth, CBL-WS) and lidar-derived z_i^{Max} , we quantified the dependence of variability of afternoon z_i on mean CBL-WS. In many studies, CBL-WS is considered an important parameter for investigating detailed eddy structures and scaling turbulence (e.g., frequency versus wavelength using CBL-WS), estimating CBL height [e.g., Stull, 1988; Choi *et al.*, 2011]. Additionally, Kaimal and Finnigan [1994] illustrated typical profiles of thermodynamic variables including CBL-WS over land in midlatitudes during cloudless conditions. Their study also documented well the features of horizontal wind speed in the surface layer, well-mixed CBL and FA, based on which we estimated the daily mean CBL-WS from radiosonde profiles.

We estimated average wind speed within the altitudes between 100 m and the middle of the z_i (often referred to as the CBL interior) obtained with the radiosonde measurements at Trappes where M10 GPS sondes obtained from Meteomodem Inc. are used on a daily basis. No vertical averaging or smoothing is applied while acquiring wind measurements at 1 Hz rate with a horizontal wind speed accuracy of 0.15 m s^{-1} and direction accuracy of 2° . For brevity, we did not consider the wind speed beyond $0.5z_i$ so that the mean CBL-WS is not affected by wind shear and veering often present in the entrainment zone near z_i .

Conditional sampling analyses were performed between the anomalies of SHF and z_i^{Max} for positive and negative CBL-WS anomaly conditions (Figure 13). Clearly seen is that for negative CBL-WS anomalies (i.e., weak CBL-WS conditions), a higher correlation coefficient and gradient were found (r of 0.48 and of γ of 1.47 m/W m^{-2}) compared to the cases with positive CBL-WS anomalies (strong CBL-WS conditions) with r

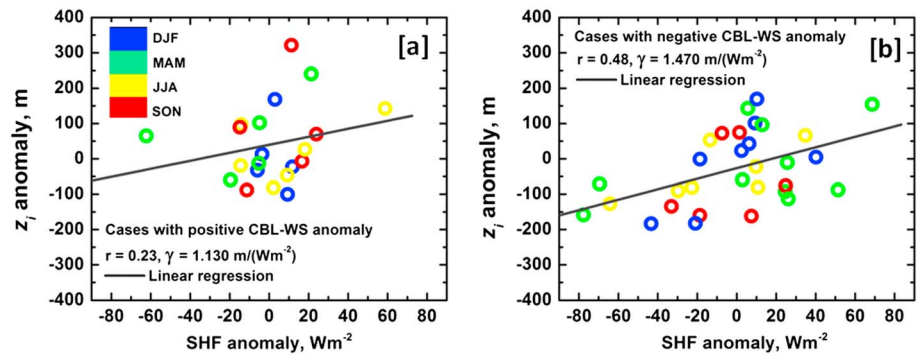


Figure 13. Scatterplot showing the relationship between the anomalies of z_i and SHF with mean boundary layer wind speed anomalies as constraint; (a) positive and (b) negative anomalies being treated separately. Each data point denotes anomalies for a particular season. The gray dashed line represents the linear regression. Corresponding correlation coefficients and gradients (γ) are also indicated.

of 0.23 and of γ of 1.13 m/W m^{-2} . These results suggest that under low CBL-WS conditions, z_i^{Max} values are more correlated to SHF conditions. Again, in summer, under low CBL-WS conditions, negative (positive) SHF anomalies coincide with negative (positive) z_i anomalies.

It should be noted, however, that the time of radiosonde launches most often do not coincide with the time when the z_i reaches its daytime “plateau” as the radiosonde launch at Trappes takes place around local noon, while lidar-derived z_i^{Max} was often found in the late afternoon. In addition, the influence of other factors, such as (1) distance between the lidar and radiosonde sites as Trappes is located 12 km west of SIRTAs so that sampling of different air masses might occur, (2) drift of the radiosonde yielding nonrepresentative CBL-WS over SIRTAs, and (3) horizontal advection cannot be completely ruled out as was previously found for measurements at SIRTAs and Trappes [e.g., Haeffelin et al., 2012; Pal et al., 2012, 2013].

Additionally, some researchers investigated the impact of advection on the local boundary layer and z_i variability over a site [e.g., Angevine et al., 2003]. Thus, we consider that along with CBL-WS, investigation of the temporal evolution of wind speed and directions at different layers, in particular in the RL during morning transition period, would be interesting to determine the impact of adjacent urban CBL (here Paris) on the z_i over a suburban site (here SIRTAs). In particular, it would be interesting to further examine what role such different horizontal wind regimes play in the variability of z_i at SIRTAs. In fact, a Doppler lidar has been recently installed at SIRTAs; concurrent measurements of aerosol and Doppler lidars in the future will be helpful in this regard to further investigate the impact of CBL-WS, wind directions, and shear on z_i variability and growth rate as was previously performed by Conzemius and Fedorovich [2006], however, using LES. In this paper, we emphasized on the potential of aerosol lidar measurements for exploring long-term z_i monitoring.

5. Summary and Conclusions

We presented a climatology on the variability of key parameters of the ABL diurnal cycle, namely, the daytime maximum z_i , the z_i growth rate, and the ABL growth duration. A long-term data set of z_i was obtained by applying a robust z_i retrieval algorithm (STRAT+) on the lidar-derived backscatter profiles obtained between October 2008 and September 2013. We also explored how other parameters may force the variability of ABL parameters at seasonal and interannual timescales. These analyses are based on the SIRTAs Re-OBS data set that contains over 40 atmospheric parameters including z_i , solar irradiance incident on the surface, SHF, T_{2m} and RH_{2m} , soil moisture, longwave cloud radiative effect, and boundary layer mean wind speed observed at the SIRTAs observatory with a 1 h time step since 2003. By analyzing monthly-mean diurnal cycle composites of z_i and different meteorological parameters, we noted that the near-surface thermodynamics plays an integral role in governing the z_i on diurnal, seasonal, and interannual timescales.

We found that variability on day-to-day, seasonal and interannual timescales of the three ABL parameters can be characterized as follows. z_i^{Max} varies from 100 to 3000 m in all seasons, with very high day-to-day

Table 3. Summary of the Conditional Sampling and Regression Analyses Discussed in Section 4.3

Conditional Sampling Between the Monthly Anomalies of SHF and z_i^{Max}		Correlation Coefficient r	Gradient γ (m/W m^{-2})
Soil moisture	Wet soil regime	0.14	0.907
	Dry soil regime	0.43	1.81
LWCRF	Occurrence of less CBL clouds	0.35	1.25
	Occurrence of more CBL clouds	0.49	1.98
CBL-WS	Higher wind speed scenarios	0.23	1.13
	Lower wind speed scenarios	0.48	1.47

variability. Largest distributions are found in spring and autumn, due to occurrence of both warm clear days and cold overcast days in those seasons. Seasonal mean values of z_i^{Max} , however, follow a well-defined seasonal cycle with 1633, 1947, 1439, and 1033 m for spring, summer, autumn, and winter, respectively. Similarly, ABL growth rate ranges from ~ 50 to more than 600 m h^{-1} in all seasons. Low growth rates ($< 100 \text{ m h}^{-1}$) and high growth rates ($> 300 \text{ m h}^{-1}$) can be found in all seasons. The distribution of growth rates is, however, very different in winter, with a median value near 112 m h^{-1} , while summer is characterized by a mean 247 m h^{-1} (median 220 m h^{-1}) growth rate. Growth duration of ABL ranges between 1 and 12 h throughout the year. All seasons have similar variability in the distribution of growth duration with mean values around 7, 8, 6, and 4 h for spring, summer, autumn, and winter, respectively. The diurnal and the seasonal z_i patterns observed over the site are similar though not identical to other European sites.

While investigating the cotemporal variations of monthly-mean z_i^{Max} with other parameters, we found that monthly-mean z_i^{Max} , solar irradiation incident on the surface, surface heat flux, and 2 m temperature are characterized by an annual cycle with similar features. This is expected, as they are all driven, on the first order, by the solar zenith angle annual cycle, and subsequent heating of the surface. Both midday $\text{RH}_{2\text{m}}$ and soil moisture show an annual cycle that is anticorrelated to monthly-mean z_i^{Max} values. In particular, monthly-mean z_i^{Max} and SSWD show a strong linear correlation ($r = 0.92$) due to the large variation of both parameters from low values in winter to high values in summer. Dispersions of residuals around the mean correlation are lowest in spring and summer and highest for winter.

Monthly-mean z_i^{Max} and SHF are also found to be correlated, but not strongly linear. Surface SHF are lowest in winter and then followed by autumn and spring. However, summer time monthly-mean SHFs are of the same magnitude as spring values, while monthly-mean z_i^{Max} in summer are larger than in spring. So while surface SHF is considered an important factor of ABL development, it is insufficient to explain the monthly variations of z_i^{Max} since other factors such as entrainment velocity and subsidence also play important roles in modulating z_i variability.

Next, we analyzed deseasonalized variations (i.e., monthly-mean anomalies) of z_i^{Max} , SSWD, SHF, 2 m temperature, longwave cloud radiative forcing, and mean CBL-WS. Corresponding results revealed three distinct periods during the 5 years in terms of z_i^{Max} values. The year 2009 until mid-2010 is characterized by positive anomalies; mid-2010 until end of 2011 is characterized by alternating positive and negative anomalies; 2012 and 2013 are characterized by negative anomalies. In a general sense, surface SHF and 2 m temperature also reveal three periods with contrasted anomalies, but correlations with z_i^{Max} anomalies are not evident. The key findings from the conditional sampling analyses are presented in Table 3.

When performing regression analysis between anomalies of monthly-mean z_i^{Max} and solar surface irradiation, we find virtually no correlation. Hence, the processes responsible for solar surface irradiation anomalies are not direct forcing factor for z_i^{Max} anomalies. We found, however, that deseasonalized variations of z_i^{Max} are somewhat correlated with monthly-mean SHF anomalies ($r = 0.38$), yet with significant scatter. Next, we found that the correlation between z_i^{Max} anomalies and SHF anomalies is sensitive to conditional sampling of surface moisture, cloud radiative forcing, and mean boundary layer wind speed values. The correlations between z_i^{Max} anomalies and SHF anomalies are stronger for dry soil moisture conditions and for negative anomalies of wind speed. This is more evident in summer than in other seasons. These conditions represent situations when SHF plays a more dominant role in the forcing of CBL development. Conversely, in conditions of high soil moisture and positive wind speed anomalies, SHF anomalies are more weakly linked to z_i^{Max} anomalies. The effect of cloud cover anomalies on the correlation between SHF and z_i^{Max} anomalies is not

straightforward. Our results show that in summer, SHF and z_i^{Max} anomalies are more correlated for negative cloud cover anomalies (less clouds).

6. Future Investigations

In this work, the potential of vertically pointing aerosol lidar measurements (so far most widely used by the scientific community) was explored for the long-term monitoring of z_i and for the investigation of near-surface meteorological processes attributing z_i variability on diurnal/seasonal/interannual timescales. However, this paper certainly did not deal with a detailed discussion on the roles of synoptic scale features, horizontal convergence, mesoscale circulations, large-scale advection, lower tropospheric stability, differential temperature advection, long-range aerosol transports, and subsidence on z_i variability which are considered potential future research topics in this field. Other ground-based remote sensing instruments at SIRTA (e.g., microwave radiometer, Doppler lidar, and ceilometer) measure a suite of thermodynamic variables during the entire diurnal cycle during different seasons which will help investigate further the dynamics and mixing processes at, over, and within the ABL. However, it should be mentioned here that the Doppler lidar data sets collected at SIRTA were not continuous as the aerosol lidar observations for the entire 5 year period (2009–2013) since SIRTA started acquiring harmonized Doppler lidar and aerosol lidar measurements only in 2011. Additionally, the role of cloud radiative effects on z_i variability could be explored further by analyzing lidar profiles but requires more assumptions (e.g., which part of the atmospheric column should be accounted for) and a more complex analysis, which is beyond the scope of our study as was performed by Dupont *et al.* [2008], among others.

Additionally, one cannot avoid impact of advection while dealing with long-term data sets. This calls for future investigation of synoptic situations which can also contribute to the variability in z_i [e.g., Bianco *et al.*, 2011]. Blay-Carreras *et al.* [2014] found that the presence of large-scale subsidence can result in z_i decreases of 200 m between the midafternoon and early evening. SIRTA z_i data set as it continues will be a suitable candidate to produce an observational climatology in future research. The linear regression analyses that we presented using the deseasonalized data (anomalies) using conditional sampling provide hints about the roles of different forcing for the boundary layer height development. Since multiple factors act together, one-to-one relationships do not reveal high correlation so that the linear regression approach considered here resulted in $r < 0.5$ (Table 3). In the future, we plan to apply other statistical tools like factor separation approach and multiparameter regression analyses to explore further the impact of near-surface thermodynamics on the z_i variability on diurnal, seasonal, and interannual timescales.

Acknowledgments

This work was funded by the SIRTA project “Multi-instruments soundings of diurnal cycle of ABL.” Most of the work was performed when one of the authors (S.P.) was affiliated with Laboratoire de Météorologie Dynamique (LMD), CNRS-Ecole Polytechnique, Palaiseau, France. We would like to acknowledge Marc-Antoine Drouin for providing the ABL height time series, Marjolaine Chiriaco and Jean-Charles Dupont for providing the SIRTA Re-OBS data set, and the SIRTA technical staff for continuously performing all the measurements. We also appreciate SIRTA members for their support during development and maintenance of a robust database for web-based interface. The data sets obtained at the SIRTA observatory are accessible for public research and teaching applications following SIRTA data policy (see <http://sirta.ipsl.fr/>). We also want to thank three anonymous reviewers for their constructive criticisms and helpful suggestions.

References

- Amiridis, V., *et al.* (2015), LIVAS: A 3-D multi-wavelength aerosol/cloud climatology based on CALIPSO and EARLINET, *Atmos. Chem. Phys. Discuss*, *15*, 2247–2304.
- Angevine, W. M., A. B. White, C. J. Senff, M. Trainer, R. M. Banta, and M. A. Ayoub (2003), Urban–rural contrasts in mixing height and cloudiness over Nashville in 1999, *J. Geophys. Res.*, *108*(D3), 4092, doi:10.1029/2001JD001061.
- Baars, H., A. Ansmann, R. Engelmann, and D. Althausen (2008), Continuous monitoring of the boundary-layer top with lidar, *Atmos. Chem. Phys.*, *8*, 7281–7296.
- Banks, R. F., J. Tiana-Alsina, F. Rocadenbosch, and J. M. Baldasano (2015), Performance evaluation of the boundary-layer height from lidar and the Weather Research and Forecasting model at an urban coastal site in the north-east Iberian Peninsula, *Boundary Layer Meteorol.*, *157*, 265–292.
- Behrendt, A., S. Pal, V. Wulfmeyer, A. M. Valdebenito, and G. Lammel (2011), A novel approach for the characterization of transport and optical properties of aerosol particles near sources—Part I: Measurement of particle backscatter coefficient maps with a scanning UV lidar, *Atmos. Environ.*, *45*, 2795–2802.
- Bianco, L., I. V. Djalaova, C. W. King, and J. M. Wilczak (2011), Diurnal evolution and annual variability of boundary-layer height and its correlation to other meteorological variables in California’s Central Valley, *Boundary Layer Meteorol.*, *140*, 491–511.
- Blay-Carreras, E., *et al.* (2014), Role of the residual layer and large-scale subsidence on the development and evolution of the convective boundary layer, *Atmos. Chem. Phys.*, *14*, 4515–4530.
- Chen, W., H. Kuze, A. Uchiyama, Y. Suzuki, and N. Takeuchi (2001), One-year observation of urban mixed layer characteristics at Tsukuba, Japan using a micro pulse lidar, *Atmos. Environ.*, *35*, 4273–4280.
- Cheruy, F., A. Campoy, J. C. Dupont, A. Ducharme, F. Hourdin, M. Haefelin, M. Chiriaco, and A. Idelkadi (2013), Combined influence of atmospheric physics and soil hydrology on the simulated meteorology at the SIRTA atmospheric observatory, *Clim. Dyn.*, *40*, 2251–2269.
- Chiriaco, M., S. Bastin, P. Yiou, M. Haefelin, J.-C. Dupont, and M. Stéfanon (2014), European heatwave in July 2006: Observations and modeling showing how local processes amplify conducive large-scale conditions, *Geophys. Res. Lett.*, *41*, 5644–5652, doi:10.1002/2014GL060205.
- Choi, W., I. C. Faloona, M. McKay, A. H. Goldstein, and B. Baker (2011), Estimating the atmospheric boundary layer height over sloped, forested terrain from surface spectral analysis during BEARPEX, *Atmos. Chem. Phys.*, *11*, 6837–6853.
- Collaud Coen, M., C. Praz, A. Haeffele, D. Ruffieux, P. Kaufmann, and B. Calpini (2014), Determination and climatology of the planetary boundary layer height by in-situ and remote sensing methods as well as the COSMO model above the Swiss plateau, *Atmos. Chem. Phys. Discuss*, *14*, 15,419–15,462.

- Conzemius, R. J., and E. Fedorovich (2006), Dynamics of sheared convective boundary layer entrainment. Part I: Methodological background and large-eddy simulations, *J. Atmos. Sci.*, *63*, 1151–1178.
- De Tomasi, F., and M. R. Perrone (2006), PBL and dust layer seasonal evolution by lidar and radiosounding measurements over a peninsular site, *Atmos. Res.*, *80*, 86–103.
- Denning, A. S., N. Zhang, C. Yi, M. Branson, K. J. Davis, J. Kleist, and P. Bakwin (2008), Evaluation of modeled atmospheric boundary layer depth at the WLEF tower, *Agric. For. Meteorol.*, *148*, 206–215.
- Di Giuseppe, F., A. Riccio, L. Caporaso, G. Bonafé, G. P. Gobbi, and F. Angelini (2012), Automatic detection of atmospheric boundary layer height using ceilometer backscatter data assisted by a boundary layer model, *Q. J. R. Meteorol. Soc.*, *138*, 649–663.
- Dupont, J., M. Haeffelin, and C. N. Long (2008), Evaluation of cloudless-sky periods detected by shortwave and longwave algorithms using lidar measurements, *Geophys. Res. Lett.*, *35*, L10815, doi:10.1029/2008GL033658.
- Granados-Muñoz, M. J., F. Navas-Guzmán, J. A. Bravo-Aranda, J. L. Guerrero-Rascado, H. Lyamani, J. Fernández-Gálvez, and L. Alados-Arboledas (2012), Automatic determination of the planetary boundary layer height using lidar: One-year analysis over southeastern Spain, *J. Geophys. Res.*, *117*, D18208, doi:10.1029/2012JD017524.
- Haeffelin, M., et al. (2012), Evaluation of mixing-height retrievals from automated profiling lidars and ceilometers in view of future integrated networks in Europe, *Boundary Layer Meteorol.*, *2012*(143), 49–75.
- Haman, C. L., B. Lefer, and G. A. Morris (2012), Seasonal variability in the diurnal evolution of the boundary layer in a near-coastal urban environment, *J. Atmos. Oceanic Technol.*, *29*, 697–710.
- He, Q., J. Mao, J. Chen, and Y. Hu (2006), Observational and modeling studies of urban atmospheric boundary-layer height and its evolution mechanisms, *Atmos. Environ.*, *40*(6), 1064–1077.
- Janssen, R. H. H., J. Arellano, L. N. Ganzeveld, P. Kabat, J. L. Jimenez, D. K. Farmer, C. C. Heerwaarden, and I. Mammarella (2012), Combined effects of surface conditions, boundary layer dynamics and chemistry on diurnal SOA-evolution, *Atmos. Chem. Phys.*, *12*, 9331–9375.
- Kafle, D. N., and R. L. Coulter (2013), Micropulse lidar-derived aerosol optical depth climatology at ARM sites worldwide, *J. Geophys. Res. Atmos.*, *118*, 7293–7308.
- Kaimal, J., and J. Finnigan (1994), *Atmospheric Boundary Layer Flows*, Oxford Univ. Press, New York.
- Ketterer, C., P. Zieger, N. Bukowiecki, M. Collaud Coen, O. Maier, D. Ruffieux, and E. Weingartner (2014), Investigation of the planetary boundary layer in the Swiss Alps using remote sensing and in-situ measurements, *Boundary Layer Meteorol.*, *151*, 317–334.
- Korhonen, K., et al. (2014), Atmospheric boundary layer top height in South Africa: Measurements with lidar and radiosonde compared to three atmospheric models, *Atmos. Chem. Phys.*, *14*, 4263–4278.
- Lac, C., R. P. Donnelly, V. Masson, S. Pal, S. Riette, S. Donier, S. Queguiner, G. Tanguy, L. Ammoura, and I. Xueref-Remy (2013), CO₂ dispersion modelling over Paris region within the CO₂-MEGAPARIS project, *Atmos. Chem. Phys.*, *13*, 4941–4961.
- Lewis, J. R., E. J. Welton, A. M. Molod, and E. Joseph (2013), Improved boundary layer depth retrievals from MPLNET, *J. Geophys. Res. Atmos.*, *118*, 9870–9879.
- Liu, S., and X. Z. Liang (2010), Observed diurnal cycle climatology of planetary boundary layer height, *J. Clim.*, *23*, 5790–5809.
- Luo, T., R. Yuan, and Z. Wang (2014), Lidar-based remote sensing of atmospheric boundary layer height over land and ocean, *Atmos. Meas. Tech.*, *7*, 173–182.
- Matthias, V., and J. Bösenberg (2002), Aerosol climatology for the planetary boundary layer derived from regular lidar measurements, *Atmos. Res.*, *63*(3–4), 221–245.
- Milroy, C., et al. (2012), An assessment of pseudo-operational ground-based light detection and ranging sensors to determine the boundary-layer structure in the coastal atmosphere, *Adv. Meteorol.*, *18*, 929080, doi:10.1155/2012/929080.
- Molod, A., H. Salmun, and M. Dempsey (2015), Estimating planetary boundary layer heights from NOAA profiler network wind profiler data, *J. Atmos. Oceanic Technol.*, *32*, 1545–1561, doi:10.1175/JTECH-D-14-00155.1.
- Morille, Y., M. Haeffelin, P. Drobinski, and J. Pelon (2007), STRAT: An automated algorithm to retrieve the vertical structure of the atmosphere from single-channel lidar data, *J. Atmos. Oceanic Technol.*, *24*, 761–775.
- Nilsson, E., D. Rannik, U. Kulmala, M. Buzorius, and C. O'Dowd (2001), Effects of the continental boundary layer evolution, convection, turbulence and entrainment on aerosol formation, *Tellus*, *53B*, 441–461.
- Pal, S. (2014), Monitoring depth of shallow atmospheric boundary layer to complement lidar measurements affected by partial overlap, *Remote Sens.*, *6*, 8468–8493.
- Pal, S., and P. C. S. Devara (2012), A wavelet-based spectral analysis of long-term time series of optical properties of aerosols obtained by lidar and radiometer measurements over an urban station in Western India, *J. Atmos. Sol. Terr. Phys.*, *84*, 75–87.
- Pal, S., A. Behrendt, and V. Wulfmeyer (2010), Elastic-backscatter-lidar-based characterization of the convective boundary layer and investigation of related statistics, *Ann. Geophys.*, *28*, 825–847.
- Pal, S., et al. (2012), Spatio-temporal variability of the atmospheric boundary layer depth over the Paris agglomeration: An assessment of the impact of the urban heat island intensity, *Atmos. Environ.*, *63*, 261–275.
- Pal, S., M. Haeffelin, and E. Batchvarova (2013), Exploring a geophysical process-based attribution technique for the determination of the atmospheric boundary layer depth using aerosol lidar and near-surface meteorological measurements, *J. Geophys. Res. Atmos.*, *118*, 9277–9295, doi:10.1002/jgrd.50710.
- Pal, S., T. R. Lee, S. Phelps, and S. F. J. De Wekker (2014), Impact of atmospheric boundary layer depth variability and wind reversal on the diurnal variability of aerosol concentration at a valley site, *Sci. Total Environ.*, *496*, 424–434.
- Pal, S., M. Lopez, M. Schmidt, M. Ramonet, I. Xueref-Remy, and P. Ciais (2015), Investigation of the atmospheric boundary layer height variability and its impact on the ²²²Rn concentration over a rural background site in France, *J. Geophys. Res. Atmos.*, *120*, 623–643, doi:10.1002/2014JD022322.
- Pan, H.-L., and L. Mahrt (1987), Interaction between soil hydrology and boundary layer development, *Boundary Layer Meteorol.*, *38*, 185–202.
- Paris, J. D., et al. (2014), Integrated Carbon Observing system: Greenhouse gas observations for GEO greenhouse gas observations for GEO and Copernicus, 8th GEO European Projects Workshops, Athens, 12–13 June. [Available at <http://www.gepw8.noaa.gov>.]
- Pedros, R., V. Estellés, M. Sicard, J. L. Gómez-Amo, M. P. Utrillas, J. A. Martínez-Lozano, F. Rocadenbosch, C. Pérez, and J. M. Baldasano (2010), Climatology of the aerosol extinction-to-backscatter ratio from Sun-photometric measurements, *IEEE Trans. Geosci. Remote Sens.*, *48*, 237–249.
- Pichelli, E., R. Ferretti, M. Cacciani, A. M. Siani, V. Ciardini, and T. Di Iorio (2014), The role of urban boundary layer investigated with high-resolution models and ground-based observations in Rome area: A step towards understanding parameterization potentialities, *Atmos. Meas. Tech.*, *7*, 315–332.

- Pino, D., J. V. G. de Arellano, A. Comer'ón, and F. Rocadenbosch (2004), The boundary layer growth in an urban area, *Sci. Total Environ.*, 334–335, 207–213.
- Raupach, M. R., and J. J. Finnigan (1995), Scale issues in boundary-layer meteorology: Surface energy balances in heterogeneous terrain, *Hydrol. Processes*, 9, 589–612.
- Sawyer, V., and Z. Li (2013), Detection, variations and intercomparison of the planetary boundary layer depth from radiosonde, lidar and infrared spectrometer, *Atmos. Environ.*, 79, 518–528.
- Schween, J. H., A. Hirsikko, U. Löhnert, and S. Crewell (2014), Mixing-layer height retrieval with ceilometer and Doppler lidar: From case studies to long-term assessment, *Atmos. Meas. Tech.*, 7, 3685–3704.
- Stull, R. B. (1988), *An Introduction to Boundary Layer Meteorology*, 666 pp., Kluwer Acad., Dordrecht.
- van der Kamp, D., and I. McKendry (2010), Diurnal and seasonal trends in convective mixed-layer heights estimated from two years of continuous ceilometer observations in Vancouver, BC, *Boundary Layer Meteorol.*, 137, 459–475.
- Vilà-Guerau de Arellano, J., K. van den Dries, and D. Pino (2009), On inferring isoprene emission surface flux from atmospheric boundary layer concentration measurements, *Atmos. Chem. Phys.*, 9, 3629–3640.
- Vilà-Guerau de Arellano, J., E. G. Patton, T. Karl, K. van den Dries, M. C. Barth, and J. J. Orlando (2011), The role of boundary layer dynamics on the diurnal evolution of isoprene and the hydroxyl radical over tropical forests, *J. Geophys. Res.*, 116, D07304, doi:10.1029/2010JD014857.
- Yang, D. W., C. Li, A. K.-H. Lau, and Y. Li (2013), Long-term measurement of daytime atmospheric mixing layer height over Hong Kong, *J. Geophys. Res. Atmos.*, 118, 2422–2433.
- Yi, C., K. J. Davis, B. W. Berger, and P. S. Bakwin (2001), Long-term observations of the dynamics of the continental planetary boundary layer, *J. Atmos. Sci.*, 58, 1288–1299.
- Zhang, Y., D. J. Seidel, and S. Zhang (2013), Trends in planetary boundary layer height over Europe, *J. Clim.*, 26, 10,071–10,076.